Modeling of the damage dynamics of nanospheres exposed to x-ray free-electron-laser radiation

Stefan P. Hau-Riege*
Lawrence Livermore National Laboratory, P.O. Box 808, Livermore, California 94551, USA

Henry N. Chapman
Centre for Free-Electron Laser Science, Universität Hamburg and DESY, Notkestrasse 85, 22607 Hamburg, Germany
(Received 19 December 2007; revised manuscript received 2 March 2008; published 1 April 2008)

Atomic-resolution diffraction imaging of biological particles using x-ray free-electron lasers (XFELs) at 1 Å wavelength requires a detailed understanding of the photon-induced damage processes. We discuss how several aspects of existing continuum damage models can be tested during early operation of XFELs at lower x-ray energies in the range of 0.8–5 keV and low fluences, focusing particularly on macroscopic collective effects such as particle charging, expansion, and average ionization of nanospheres.

DOI: 10.1103/PhysRevE.77.041902 PACS number(s): 87.64.Bx, 61.05.cp, 82.53.Ps

X-ray free-electron lasers (XFELs) deliver photon pulses that are intense, short in duration, and of small wavelength. The free-electron laser in Hamburg (FLASH) is the only XFEL that is currently operating, providing photon pulses down to a wavelength of 6 nm [1]. Soon hard XFELs will become available, such as the Linac coherent light source (LCLS) in 2009 [2]. Once wavelengths of around 1 Å are achieved, atomic-resolution coherent imaging of biological molecules may be feasible [3]. In these experiments, identical molecules will be exposed to XFEL pulses one by one, and their diffraction patterns will be recorded, from which a real-space molecular image may be reconstructed.

XFEL-induced radiation damage determines the pulse requirements for imaging. Damage is initiated by photoionization of primarily the atomic *K* shell, producing high-energy photoelectrons. The excited atoms decay preferentially through Auger relaxation, resulting in the emission of medium-energy Auger electrons. Both Auger and photoelectrons escape the particle; we call these *free* electrons. On their way out of the particle the free electrons produce low-energy secondary electrons. Once the particle has accumulated sufficient positive charge, trapping of electrons occurs; these electrons are called *quasifree*. The net particle charge induces a strong Coulomb explosion. Simultaneously, but on a slower time scale, the high temperature of the quasifree electrons leads to a hydrodynamic expansion of the sample.

Precise predictions of pulse-length and fluence requirements are essential for planning diffraction imaging experiments. Several models [3–7] have been proposed to assess the effect of damage on the image quality. These models and various mitigation strategies allowing longer pulse lengths [8,9] strongly rely on an understanding of the damage physics. Early testing and validation of these models are crucial for realistic experimental designs.

Typically, XFELs become operational first at longer wavelengths since electron-injector and undulator requirements are less stringent [10]. It is anticipated that the LCLS will provide photon pulses with energies of up to a few keV initially, and only later on produce FEL radiation of up to 8 keV. In this paper we show that several key aspects of the damage physics can already be tested in the lower-energy regime. We propose to measure the diffraction pattern of exploding nanospheres at the LCLS as a function of the FEL pulse energy, and to analyze features in the diffraction patterns that are characteristic for key aspects of the explosion dynamics. We first describe our model to calculate the damage dynamics and the diffraction patterns of exploding nanoparticles. We then discuss the damage dynamics of carbon spheres when exposed to an XFEL beam as a function of pulse fluence and photon energy, and their diffraction patterns. Finally, we summarize and conclude this paper.

We used a continuum model to calculate the damage process in carbon spheres of radius $R_0=50$ Å. This size is comparable to relevant biological molecules. We have extended the model from photon energies around 8 keV [5] down to 0.8 keV. At 0.8 keV the primary x-ray–atom interaction process is still photoionization. Despite the high electromagnetic field intensity, classical electromagnetic field effects that typically occur for optical lasers [11] can still be neglected due to the small wavelength of 15 Å. The model lacks the atomic detail of molecular dynamics (MD) models [3,4,6], but has allowed us to include some additional physics that MD models until now have ignored, such as three-body electron-ion recombination. In addition, the continuum model can treat large particles, whereas the MD models have been limited to particles containing at most a few thousand atoms.

Figure 1(a) illustrates the outward motion of selected spatial shells of a carbon sphere with a mass density of 1.35 g/cm^3. During x-ray exposure, the quasifree electrons thermalize and redistribute so that the inner volume of the particle is neutral, and the outer layer is positively charged and expands rapidly. The total charge distribution is shown in Fig. 1(b). In this and all the following calculations we assume that the photon pulse contains 3×10^{11} photons at 2 keV, has a duration of 200 fs, and is focused to a full width at half maximum (FWHM) of 0.2 μm, corresponding to a photon fluence of 6.6×10^{12} photons/μm^2. These parameters are expected to be achieved during the early operation of LCLS.

The diffraction pattern of the particle is determined by the total electron density. We will now discuss the dependence of

*hauriege1@llnl.gov

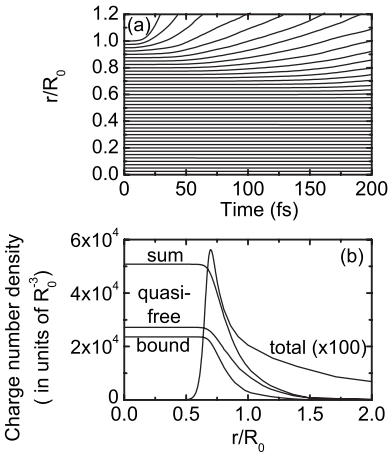

FIG. 1. (a) Motion of selected atomic shells. (b) Charge number densities of quasifree and atomically bound electrons, as well as their sum, as a function of radial position at 100 fs. Also shown is the total charge number density including the ion contribution that is responsible for the Coulomb explosion.

the electron densities, the ionization states, and the sample expansion on the x-ray energy, and how they are related to changes in the diffraction pattern. The number of escaped electrons and the onset of charge trapping significantly affect the damage dynamics since they determine the particle charge, and with that the Coulomb explosion dynamics, the ionization kinetics, and the temperature of the quasifree electrons. Whereas secondary and Auger electrons are trapped early on in the exposure to the XFEL beam, a significant fraction of the higher-energy photoelectrons escape. Figure 2 shows the number of escaped electrons N_f as a function of the x-ray energy E_{xray} ranging from 0.8 to 8 keV, for beam diameters of 2.0, 1.0, 0.5, and 0.2 μm FWHM, corresponding to photon fluences of 6.6×10^{10}, 2.6×10^{11}, 1.1×10^{12}, and 6.6×10^{12} photons/μm^2, respectively. N_f first increases with E_{xray}, reaches a maximum, and decreases again. This is due to trapping of some photoelectrons for small values of E_{xray}, and the escape of all photoelectrons beyond the maximum: Neglecting the expansion dynamics of the particle and the small fraction of Auger electrons escaping the particle initially, photoelectrons originating near the particle surface are trapped when the charge of the particle reaches a critical

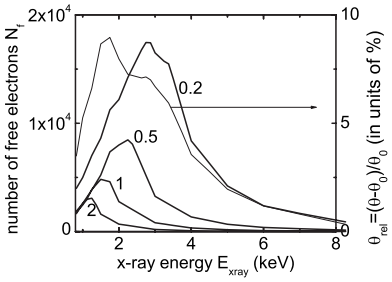

FIG. 2. Number of escaped electrons as a function of x-ray photon energy. The numbers indicate the FWHM of the beam in micrometers. Overlaid is the relative change in the position of the first minimum in the diffraction pattern for a beam FWHM of 0.2 μm.

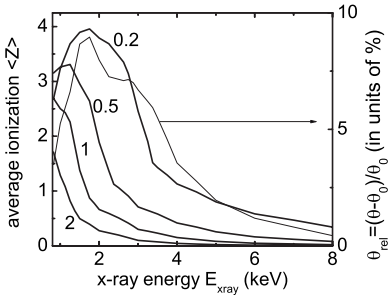

FIG. 3. Average atomic ionization at the end of the pulse as a function of x-ray photon energy E_{xray}. The numbers indicate the FWHM of the beam in micrometers. Overlaid is the relative change in the position of the first minimum in the diffraction pattern for a beam FWHM of 0.2 μm.

charge $Q_c=eN_c$ with $E_{\mathrm{photo}}=Q_c/R$. Here e is the elementary charge, N_c the critical charge number, R the radius of the particle, and $E_{\mathrm{photo}}=E_{\mathrm{xray}}-E_{\mathrm{bind}}$, where E_{bind} is the electron binding energy. For small x-ray energies, $N_f=N_c=E_{\mathrm{photo}}R/e$, and N_f is linear in E_{xray}. Once E_{xray} is sufficiently large so that trapping of the photoelectrons does not occur, N_f reaches a maximum and decreases again since then $N_f\approx I_0\sigma$; σ is the photoionization cross section, which decreases with increasing x-ray energy. For smaller fluences, the maximum in N_f occurs at smaller E_{xray} since less charge accumulates and the crossover shifts to smaller E_{xray}.

The precise dependence of N_f on E_{xray} can only be understood by considering the radial location of the origin of the photoelectrons, the escaping Auger electrons, and the details of the charge distribution, which, in turn, is determined by the ion distribution, the sample expansion, the electron temperature, and the time at which trapping occurs. For example, when the particle has expanded significantly, some electrons can escape more easily.

Figures 3 and 4 show the average ionization $\langle Z\rangle$ and the number of quasifree electrons N_{qf}, respectively, as a function of E_{xray}. The shapes of both curves are roughly similar since $N_{\mathrm{qf}}\gg N_f$, so that $\langle Z\rangle$ does not strongly depend on N_f. $\langle Z\rangle$ and N_{qf} increase with E_{xray}, reach a maximum, decrease, and then change slope (become flatter). The slope change occurs at the same x-ray energy at which N_f reaches a maximum, which, in turn, is the energy beyond which photoelectrons are not

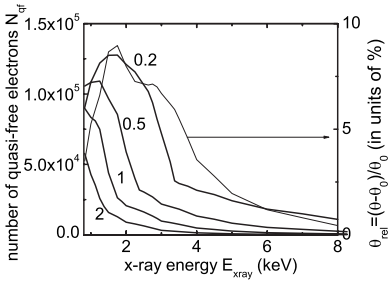

FIG. 4. Number of quasifree electrons at the end of the pulse as a function of x-ray photon energy. The numbers indicate the FWHM of the beam in micrometers. Overlaid is the relative change in the position of the first minimum in the diffraction pattern for a beam FWHM of 0.2 μm.

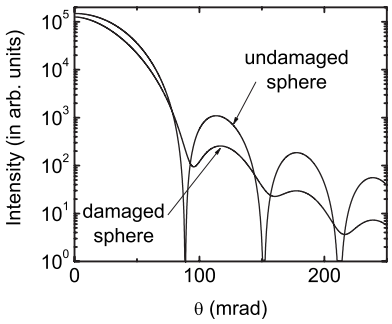

FIG. 5. Pulse-averaged diffraction pattern of an expanding sphere. Also shown is the diffraction pattern of an undamaged sphere.

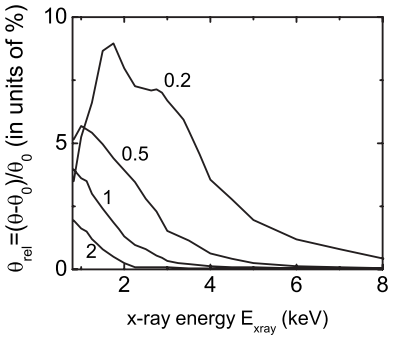

FIG. 6. Relative change in the position of the first minimum of the diffraction pattern of the expanding sphere. θ_0 and θ_1 are the positions of the first minimum of the diffraction pattern of the undamaged and damaged particles, respectively. The numbers indicate the FWHM of the beam in micrometers.

electrostatically trapped. If photoelectrons are not trapped, less electron impact ionization occurs, leading to lower $\langle Z \rangle$ and N_{qf}. The precise dependence of $\langle Z \rangle$ and N_{qf} on E_{xray} is complicated by the nonhomogeneity of the particle, three-body recombination when the electron density is large, and the different valence electron ionization energies for different charge states.

The sum of the densities of atomically bound and quasifree electrons [see Fig. 1(b)] determines the diffraction pattern. The free electrons do not contribute significantly since they make up less than 20% of the total number of electrons. The temporal coherence properties of the LCLS pulse need to be considered for calculating the diffraction patterns. A single LCLS pulse consists of several hundred self-amplification of spontaneous emission (SASE) spikes. Each spike is to a high degree temporally and spatially coherent, but the spikes do not have a well-defined phase correlation relative to each other [10]. To calculate the diffraction pattern of the expanding sphere, we calculate the diffraction patterns of 250 snapshots of the electron density during the pulse, corresponding to the diffraction pattern induced by single SASE spikes, and add the intensity of these patterns. To calculate each diffraction pattern, we project the electron density of the sphere onto a plane that is perpendicular to the x-ray beam. Since this projection is rotationally symmetric, the calculation of its Fourier transform is equivalent to calculating the Hankel transformation of a lineout.

Figure 5 shows the diffraction pattern of an expanding sphere and of the same sphere in the absence of damage. Whereas the diffraction pattern of the undamaged sphere exhibits sharp peaks, the pattern of the expanding sphere is significantly smeared out since the sphere changes during the pulse. Also, the minima have shifted to larger angles. In principle, image reconstruction algorithms could be used to extract the electron density distribution, but it is more illuminating to analyze the diffraction patterns directly to identify trends as a function of the photon energy.

Figure 6 shows the relative change in the position of the first minimum of the diffraction pattern θ_{rel} as a function of the photon energy. θ_{rel} correlates with the size of the bound and quasifree electron cloud and is a measure for the amount of damage to the particle. As apparent from Figs. 2–4, the θ_{rel} curves are wider than the N_f, $\langle Z \rangle$, and N_{qf} curves, which is a signature for different dominating damage mechanisms at different x-ray energies. For small E_{xray}, the Coulomb expansion proceeds rapidly because the outer region of the particle is strongly ionized, corresponding to large values of $\langle Z \rangle$ and N_{qf}. For larger x-ray energies, the rate of Coulomb expansion is primarily determined by the amount of positive charge on the particle (N_f). For small focal diameters of 0.2 and 0.5 μm, θ_{rel} reaches a maximum at 1.8 and 1.0 keV, respectively. The shapes of the curves are a direct measure for the degree of ionization at low x-ray energies and for the reduced tendency to trap photoelectrons at larger x-ray energies. These features occur at x-ray energies up to 4 keV and can be explored at the early LCLS operation when photon energies of only up to a few keV will be available.

In this study we have focused on particles with a radius of 50 Å. We found that the change in radius of larger particles is much smaller since many fewer electrons escape the particle. For example, a particle with a 150 Å radius changes its radius by less than 2% for all x-ray energies and the highest fluence considered. Smaller particles have the disadvantage that the scattering cross section is smaller, leading to a weaker signal, and that certain features in the diffraction patterns do not occur: For particles with a radius of 25 Å, trapping of photoelectrons is much less likely, so that the rising part of the $\theta_{\mathrm{rel}}(E_{\mathrm{xray}})$ curve as shown in Fig. 6 for 50 Å particles is not observed even for the highest fluences considered in this study. Using atoms with larger nuclear charge such as gold would produce a much stronger scattering signal, but even though the physical damage processes that occur in gold and in much lighter biological materials are similar, the relative time scales of the different processes are very different, so that such experiments would not be a good test for the damage model for biological samples.

In summary, we have predicted the explosion dynamics of carbon spheres exposed to XFEL pulses similar to the expected early operational parameters of the XFEL LCLS. We have also calculated the diffraction patterns with which the explosion dynamics can be imaged. In lieu of actually reconstructing the electron density, we propose to analyze certain features of the diffraction pattern that measure particle damage: The expansion dynamics closely relates to the onset of electrostatic trapping of the electrons, the ionization state of

the material, and the density and temperature of the quasifree electrons. Comparison to experimental data will allow for testing our understanding of the damage dynamics of particles exposed to the XFEL beam, which is pivotal for the design of diffraction imaging experiments of biological particles. Our simulations show that this comparison can be performed using photon pulses that contain 3×10^{11} photons, which is up to ten times lower than the specifications for the fully functional LCLS, since x-ray–matter interaction is much stronger at longer wavelengths. Performing these verifications early in the LCLS operation will give confidence in the pulse-length estimates and sample-size suggestions, as well as various concepts for alleviating stringent pulse requirements.

This work was performed under the auspices of the U.S. Department of Energy by Lawrence Livermore National Laboratory under Contract No. DE-AC52-07NA27344.

[1] V. Ayvazyan *et al.*, Eur. Phys. J. D **37**, 297 (2006).
[2] Linac Coherent Light Source (LCLS) Design Study Report No. SLAC-R-521, 1998, National Technical Information Services, 5285 Port Royal Road, Springfield, VA, 22161.
[3] R. Neutze, R. Wouts, D. van der Spoel, E. Weckert, and J. Hajdu, Nature (London) **406**, 752 (2000).
[4] Z. Jurek, G. Faigel, and M. Tegze, Eur. Phys. J. D **29**, 217 (2004).
[5] S. P. Hau-Riege, R. A. London, and A. Szoke, Phys. Rev. E **69**, 051906 (2004).
[6] M. Bergh, N. Timneanu, and D. van der Spoel, Phys. Rev. E **70**, 051904 (2004).
[7] B. Ziaja, A. R. B. de Castro, E. Weckert, and T. Moller, Eur. Phys. J. D **40**, 465 (2006).
[8] S. P. Hau-Riege, R. A. London, G. Huldt, and H. N. Chapman, Phys. Rev. E **71**, 061919 (2005).
[9] S. P. Hau-Riege, R. A. London, H. N. Chapman, A. Szoke, and N. Timneanu, Phys. Rev. Lett. **98**, 198302 (2007).
[10] Z. Huang and K.-J. Kim, Phys. Rev. ST Accel. Beams **10**, 034801 (2007).
[11] W. L. Kruer, *The Physics of Laser Plasma Interactions* (Westview Press, Boulder, CO, 2003).